



Current Opinion in Solid State & Materials Science

journal homepage: www.elsevier.com/locate/cossms

Chemical effects on He bubble superlattice formation in high entropy alloys

R.W. Harrison^{a,*}, G. Greaves^a, H. Le^a, H. Bei^{b,c}, Y. Zhang^{b,c}, S.E. Donnelly^a^a School of Computing and Engineering, University of Huddersfield, Queensgate, Huddersfield HD1 3DH, UK^b Materials Science and Technology Division, Oak Ridge National Laboratory, Oak Ridge, TN 37831, USA^c Department of Materials Science and Engineering, University of Tennessee, Knoxville, TN 37996, USA

ARTICLE INFO

Keywords:

High entropy alloy
Chemical complexity
Irradiation
Helium bubble superlattice
In situ TEM

ABSTRACT

The probable formation mechanism of He bubble superlattices relies on long range anisotropic diffusion of self-interstitial atoms (SIAs). Here we study He ion irradiation of pure Ni and two equiatomic concentrated solid-solution alloys (CSAs) of FeNi and FeCrNiCo. It is expected from the significantly reduced diffusion of SIAs in CSAs, including high entropy alloys (HEAs), that long range anisotropic SIA migration cannot be active. We report the formation of a He bubble lattice in pure Ni, and for the first time in FeNi and FeCrNiCo systems under 30 keV He ion irradiation at room temperature. The ion dose and flux required to form a bubble superlattice increase with chemical complexity. Comparing to Ni, SIA clusters change directions more frequently due to anisotropic elementally-biased diffusion from the higher degree of chemical non-homogeneity in CSAs. Nevertheless, anisotropic 1-D diffusion of interstitial defects is possible in these complex alloys over incrementally longer time scales and irradiation doses. The sluggish diffusion, characteristic in CSAs, leads to smaller superlattice parameters and smaller bubble diameters. The chemical biased SIA diffusion and its effects on He evolution revealed here have important implications on understanding and improving radiation tolerance over a wide range of extreme conditions.

1. Introduction

Single-phase high entropy alloys (HEAs) are part of a novel class of materials, termed single-phase concentrated solid solution alloys (SP-CSAs), that have received increasing attention in the literature with regards to their superior properties over traditional alloys [1]. The high entropy nature of these materials arises from the fact that the alloying components are in equiatomic fractions and form solid-solution, face-centred cubic (FCC) or body-centred cubic (BCC) phases. Their extraordinarily desirable properties include higher yield strengths, excellent high-temperature properties [2], good corrosion resistance [3–9] and promising radiation behaviour [10–12].

Studies of defect dynamics in FCC Ni, FeNi, NiCo and FeCrNiCo through *ab initio* electronic structure calculations, molecular dynamic (MD) simulations and room-temperature (298 K) ion irradiation (3 MeV Au⁺ ions to a fluence of 2×10^{13} ions/cm², which produced ~ 0.17 displacements per atom (DPA) at the damage peak) show that interstitial-type dislocation loops formed with an average size of ~ 7.0 nm for the elemental Ni and decreased to ~ 4.3 nm for the NiCo and FeNi alloys. The reduction in loop size is attributed to enhanced defect annealing in the SP-CSAs, and heterogeneous defect migration barriers prohibiting the growth of extended defects and larger dislocation loop

sizes [12]. Lu et al. [10] have investigated 1.5 or 3.0 MeV Ni ion irradiation of FeNi, FeNiCo, FeCrNiCo and FeCrNiCoMn at 773 K to a fluence of 5×10^{16} ions/cm². The authors noted delayed loop growth as chemical complexity increased [10], which may be attributed to the complex energy landscapes arising from the maximized site-to-site chemical disorder and, therefore, significantly modified atomic motion. Consequently, sluggish diffusion, defined as reduced defect mobility or decreased interstitial migration length, in SP-CSAs is observed.

Helium bubble and void superlattices have been reported to form in Fe [13], Cr [13] and Ni [14,15] as well as many other BCC and FCC metals [13,15–33]. Proposed formation mechanisms have been based on: elastic interaction between cavities [34], isomorphic decomposition [35], phase instability, interstitial loop punching [36], and 1-D [27] or 2-D self-interstitial atom (SIA) diffusion [28]. For the case of the anisotropic SIA migration mechanisms, cavities begin to nucleate randomly and those which are aligned with one another along the direction or plane of SIA migration will experience a shadowing effect from anisotropically migrating SIAs. Heinish and Singh [37] suggest that, for near perfect void lattices, the mean free path (L) of the SIA in the 1-D case has to be at least 2.7 times larger than the void mean nearest-neighbour distance.

As the predominant formation mechanism of bubble and void

* Corresponding author at: School of Mechanical, Aerospace and Civil Engineering, The University of Manchester, Sackville Street, Manchester M1 3NJ, UK.
E-mail address: r.w.harrison@manchester.ac.uk (R.W. Harrison).

superlattices in irradiated materials relies on the long range 1-D or 2-D diffusion of SIAs, it is anticipated that these superlattices will not form in SP-CSAs, which reportedly have intrinsic lattice distortion and very restricted interstitial mobility. We have irradiated Ni and equiatomic FeNi and FeCrNiCo samples with 30 keV He⁺ ions at 298 K in-situ in a transmission electron microscope (TEM) under conditions where bubble superlattices occur in the elemental Ni.

2. Experimental

Rods of pure Ni, FeNi and FeCrNiCo equiatomic alloys were produced by arc melting followed by drop-casting into a copper mould in an Ar atmosphere. Single crystalline rods were then grown via directional solidification in an optical floating-zone furnace under Ar gas. Further information can be found elsewhere [10–12].

Samples for TEM were prepared by the conventional Focused Ion Beam (FIB) lift-out technique (FEI Quanta 200 3D). In-situ ion irradiations were performed at the Microscopes and Ion Accelerators for Materials Investigations facility (MIAMI) utilising the MIAMI-2 system. The MIAMI-2 system consists of a 350 kV ion accelerator (NEC) coupled with a TEM (Hitachi-H9500 operated at 300 kV) in which the ion beam is incident at 18.7° with respect to the electron beam described elsewhere [38]. Samples were irradiated with 30 keV He⁺ ions at 298 K with a flux of $\sim 6 \times 10^{13}$ ions/cm²/s up to a total fluence of 4×10^{17} ions/cm². MoO₃ crystals were used to calibrate the image rotation between the diffraction patterns and micrographs.

Helium bubble ordering and the formation of the bubble superlattices were monitored and confirmed by selected area diffraction patterns (SADPs) and fast Fourier Transform (FFT) of the images. As the He superlattice forms a 3-D ordered array it gives rise to its own unique lattice spacings and thus reflections in the electron diffraction pattern providing a direct indication of He bubble superlattice formation. This is described in Fig. 1, where the schematic diagram shows how Ni lattice reflections in the SADP are subsequently re-diffracted by the He bubble lattice resulting in the appearance of satellite spots around the matrix reflections. These have a much smaller spacing in reciprocal space due to the He bubble lattice spacing being an order of magnitude larger than the matrix lattice spacing in real space. However, as the helium bubble lattice spacing is variable this can give rise to a weaker diffraction streak, rather than a discrete spot (as seen in Fig. 1) and this may be unresolvable against the high intensity matrix diffraction spot next to it. Instead, Fourier analysis of the images is a powerful method of examining periodicity in TEM images. This was performed by taking the FFT of the bubble lattice images using the Gatan Microscopy suite (GMS) version 3.0. The FFT converts the images from a spatial

representation into its sine and cosine components resulting in a distribution of frequencies of the signal [39]. A random image (such as an amorphous structure) gives a diffuse halo and repeating spatial signals give rise to repeating frequencies resulting in spots and lobes indicative of periodicity. The formation and intensity of the lobes in the FFTs thus gives powerful direct evidence of the initial formation and strengthening of the ordering as the bubble lattice becomes more developed. This may be missed by other techniques including direct visual observation.

Helium bubble diameters and bubble lattice *d*-spacings (*d*_{bubble}) were determined directly from images based on 30 measurements using GMS 3.0. All images were acquired with 1 μm of defocus and so bubble diameters are directly comparable. Helium bubble lattice parameters (*a*_{bubble}) were calculated using Eq. (1) measuring lattice spacings along *d*₂₂₀ and *d*₁₁₁ as indexed from SADPs corrected for rotation between the image and the diffraction pattern. The values of He bubble diameter and bubble lattice constant are reported as the average with the error bars representing the standard deviation (variance) from the mean.

$$a_{\text{bubble}} = d_{\text{bubble}} \sqrt{h^2 + k^2 + l^2} \quad (1)$$

An example of these measurements is given in Fig. 2. Fig. 2a shows a TEM image of a Ni sample irradiated with 30 keV He ions to a fluence of 1.5×10^{17} ions/cm² at 298 K and the formation of ordered He bubbles along {2 2 0} planes. A plot of the intensity profile is made along one of these rows (shown in Fig. 2b) and the interplanar spacing (*d*₂₂₀ of the He bubble lattice in the example) was measured between the two bright maxima (images are taken with 1 μm overfocus so bubbles appear dark). He bubble diameters were measured by drawing a line across the bubble intensity and setting the length to the edges of the bubble as the median intensity on either side of the scan through the bubble as shown in Fig. 2c and d.

3. Results

Fig. 3a and b show bright-field TEM (BF-TEM) images of a Ni sample irradiated with He ions to a fluence of 1.5×10^{17} ions/cm² taken with 1 μm overfocus. The FFT shows the presence of ordering of the bubbles (indicated by arrows). Fig. 3c shows a SADP of the region in Fig. 3a and b confirming that bubble ordering is isostructural with the host FCC structure, aligned along {2 2 0} planes and shows the formation of He bubble superlattice reflections around each matrix reflection in the <2 2 0> directions, agreeing well with the FFT and TEM images. Ordering in He bubble lattices has been reported to be most strongly evident along close packed planes in BCC and FCC materials [13,15–23,26–33]. As <1 1 0> type directions lie within {1 1 1} type

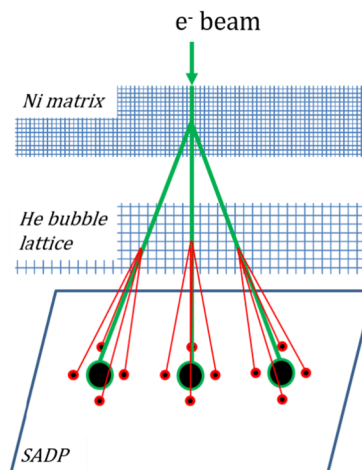
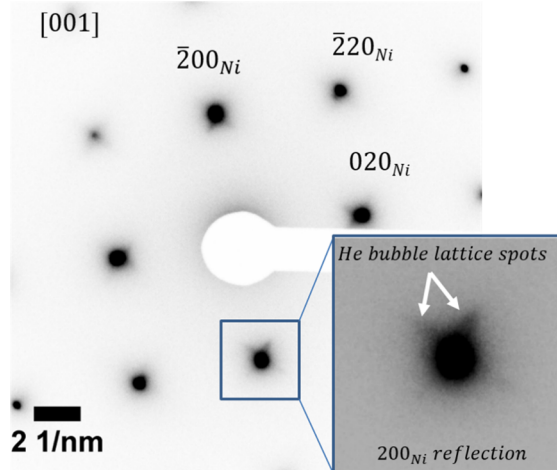


Fig. 1. SADP of a Ni sample irradiated with 30 keV He ions to a fluence of 1.5×10^{17} ions/cm² at 298 K showing formation of He bubble superlattice reflections around matrix reflections with schematic of satellite spot reflection formation in the SADP (a single set of planes is given for the Ni reflections for diagram simplicity).

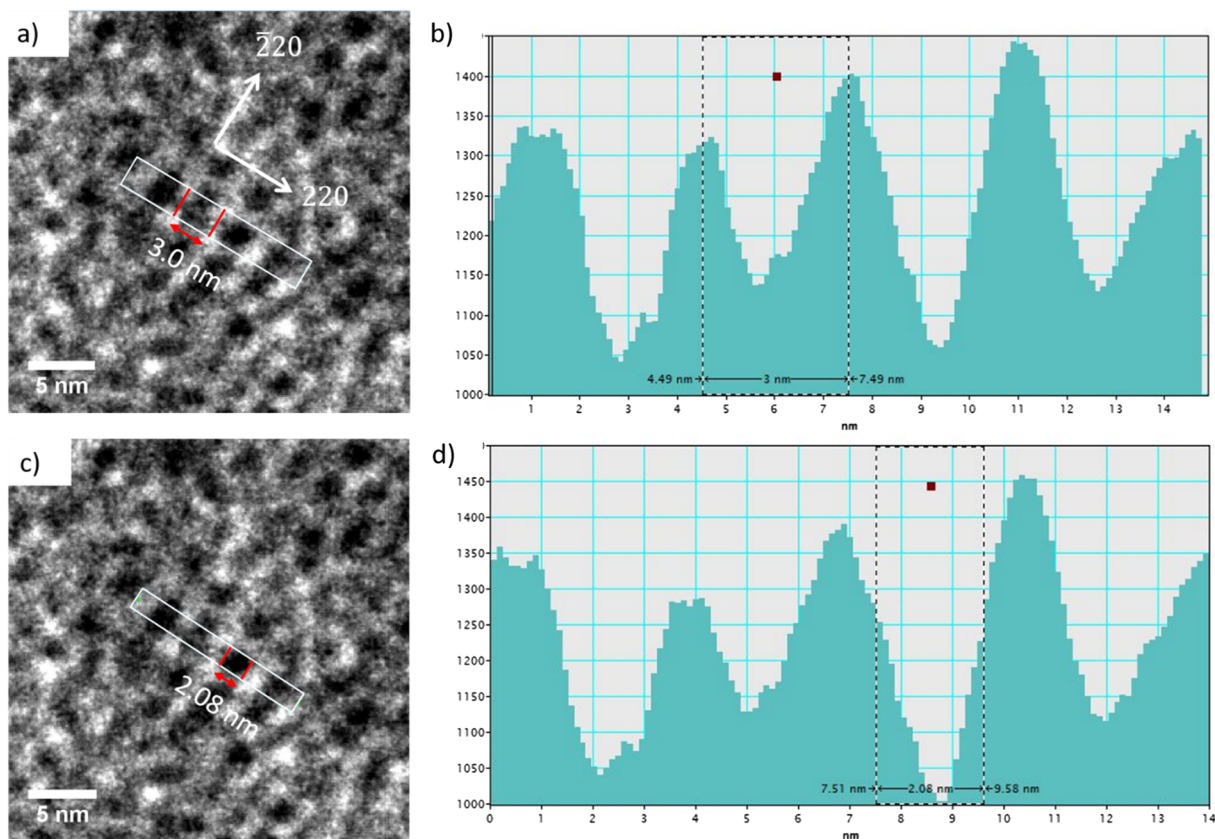


Fig. 2. Examples of measurement of (a) TEM image of a Ni sample irradiated with He 30 keV He ions to a fluence of 1.5×10^{17} ions/cm 2 at 298 K with marked bubble lattice spacing along $\{2\ 2\ 0\}$ planes, (b) plot of intensity of line drawn along $[2\ 2\ 0]$ direction, (c) the same TEM image showing bubble diameter and d) plot of intensity along profile drawn in c.

planes in the FCC structure, (for example the $[0\bar{1}1]$ direction lies within the $(1\ 1\ 1)$ plane) this gives rise to the strongest ordering being observed along $\langle 1\ 1\ 0 \rangle$ directions and so lobes shown by the FFT inset in Fig. 3a and satellite $\langle 2\ 2\ 0 \rangle$ spots in the SADP (Fig. 3c) are strongest along these crystallographic orientations.

Fig. 4 shows the evolution of the bubble lattice ordering in pure Ni irradiated with 30 keV He at 298 K showing that a lattice formed at a fluence of $\sim 8 \times 10^{16}$ ions/cm 2 and became strongly ordered at a fluence of $\sim 1.5 \times 10^{17}$ ions/cm 2 , as indicated by the stronger lobes in the FFT.

We report, for the first time, an observation of He bubble lattices formed in FeNi and FeCrNiCo. Fig. 5a and b show BF-TEM images of a He bubble lattice in the FeNi sample irradiated to a fluence of

3.1×10^{17} ions/cm 2 taken with 1 μm of objective lens overfocus. The sample was imaged close to the $[1\ 0\ 1]$ zone axis as confirmed by the SADP in Fig. 5c showing that ordering observed in the FFT and the enlarged region in Fig. 5b exhibits alignment of bubble lattice planes with the close-packed $\{1\ 1\ 1\}$ planes of the FeNi matrix as expected from the bubble lattice ordering mechanism. Bubble lattice ordering was observed at a fluence of $\sim 9 \times 10^{16}$ ions/cm 2 and the degree of ordering continued to increase until $\sim 2.5 \times 10^{17}$ ions/cm 2 as shown by the sequence of BF-TEM images and FFTs of the FeNi sample in Fig. 6.

The BF-TEM images in Fig. 7a and b show a FeCrNiCo sample after irradiation to a fluence of 4×10^{17} ions/cm 2 at 298 K taken close to the $[1\ 1\ 2]$ FCC zone axis (as confirmed by the SADP in Fig. 7c) and the FFT inset shows clear ordering along $\langle 1\ 1\ 1 \rangle$ and $\langle 1\ 1\ 0 \rangle$ directions. The

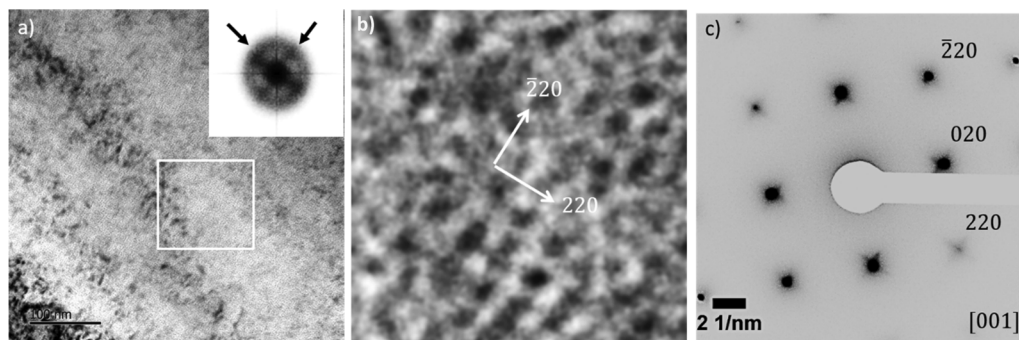


Fig. 3. Ni sample irradiated with 30 keV He ions to a fluence of 1.5×10^{17} ions/cm 2 at 298 K. (a) BF-TEM image of a helium bubble lattice taken with 1 μm of overfocus. Imaged close to $[0\ 0\ 1]$ zone axis, FFT inset shows lobes (indicated by arrows) showing alignment along $\langle 1\ 1\ 0 \rangle$ directions. (b) enlarged image of region inside white box in a, in which the satellite spots associated with each of the matrix reflections arise from diffraction from bubble lattice planes coincident with Ni $\{2\ 2\ 0\}$ planes confirmed with “lobes” present in the FFT associated with He bubble lattice ordering along $\langle 1\ 1\ 0 \rangle$ directions. (c) SADP of region shown in a and b, in which the satellite spots associated with each of the matrix reflections arise from diffraction from bubble lattice planes coincident with Ni $\{2\ 2\ 0\}$ planes confirmed with “lobes” present in the FFT associated with He bubble lattice ordering along $\langle 1\ 1\ 0 \rangle$ directions.

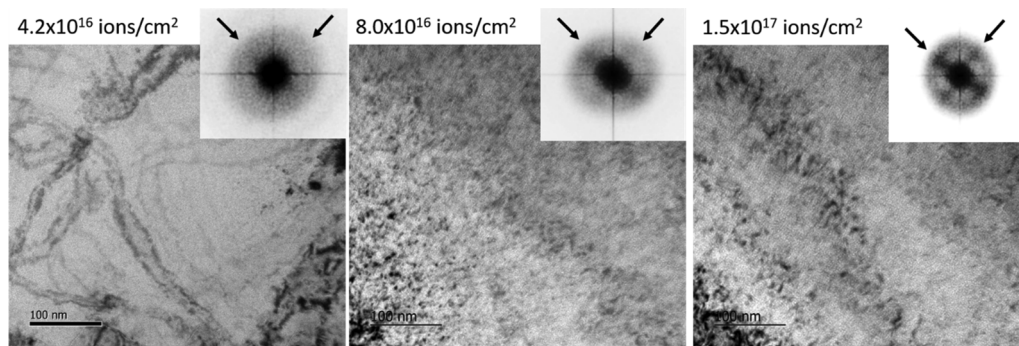


Fig. 4. Evolution of He bubble lattice ordering in a pure Ni sample (imaged close to [0 0 1] zone axis) as a function of increasing He ion fluence, showing that ordering into a bubble lattice can be seen in the FFT due to the formation of lobes along $\langle 110 \rangle$ directions (indicated by arrows) from a fluence of $8 \times 10^{16} \text{ ions/cm}^2$ and is clearly visible at a fluence of $1.5 \times 10^{17} \text{ ions/cm}^2$. Images have been recorded with $1 \mu\text{m}$ of underfocus.

alignment of the helium bubble lattice with the FCC matrix is also shown in Fig. 7d/e (BF-TEM images) and Fig. 7f (SADP) of the FeCrNiCo sample imaged close to the [1 0 1] zone axis. The FFT inset in Fig. 7d shows clear ordering of bubbles along the close-packed $\langle 111 \rangle$ directions. He bubble lattices were observed to form at a fluence of $\sim 1.1 \times 10^{17} \text{ ions/cm}^2$ in the FeCrNiCo alloy, higher than the doses required to form a bubble lattice in either the pure Ni or the FeNi alloy. The ordering of the bubble lattice improved with increasing fluence to $\sim 3.6 \times 10^{17} \text{ ions/cm}^2$, as shown in Fig. 8.

4. Discussion

4.1. On the formation of the bubble lattice

The observation of bubble ordering along close packed planes provides important insights into the mechanism by which bubble lattices are formed [33]. Long range anisotropic migration of SIAs will occur either in 1-D or 2-D along close packed directions or close packed planes, respectively, resulting in the bubble lattice being isostructural with the matrix. In BCC materials, where the lowest energy SIA configuration is the $\langle 111 \rangle$ crowdion, a mechanism of 1-D diffusion along close packed $\langle 111 \rangle$ directions may easily be applied [40]. The formation energy of the $\langle 110 \rangle$ dumbbell in BCC W is a fraction of an eV higher than the $\langle 111 \rangle$ crowdion (9.84 and 9.55 eV respectively [41,42] and 2-D diffusion of this dumbbell along $\{110\}$ type planes may also be envisaged [23]. Low energy SIA configurations are required as migration needs to be restricted along 1-D axes or 2-D planes without rotation onto another equivalent type axis, which would give rise to 3-D migration.

For an FCC lattice, the close packed directions and planes are $\langle 110 \rangle$ type directions and $\{111\}$ type planes, respectively. The lowest energy SIA for an FCC lattice is the $\langle 001 \rangle$ type [20], which is common to two $\{001\}$ planes, excluding anisotropic migration. It has been proposed that, under anisotropic stresses, the $\langle 001 \rangle$ SIA may be constrained to anisotropic migration [28,43]. However, this would result in a simple cubic structure, not the FCC lattice observed in the current and previous works [14,15,43]. Evans [28] has proposed that a $\langle 112 \rangle$ dumbbell would give the correct symmetry in the FCC lattice for

anisotropic diffusion but queried whether this would be a possible low-energy configuration. However, Beeler [44] suggested that a planar crowdion configuration on the close packed (111) plane which migrates within that plane (i.e. along $\langle 110 \rangle$ directions) would give rise to the correct FCC cavity lattice. Gao et al. [45] have also suggested that the diffusing planar defects are SIA clusters migrating along $\langle 110 \rangle$ directions, which give rise to the FCC cavity lattice. Evans [32] has also proposed that the planar migrating defect must be a di-interstitial as the simulations involving the mono-interstitial predicted cavity lattices at much lower DPAs than were observed experimentally. Thus, the di-interstitial or small interstitial clusters (SIA clusters), which are present in a much lower concentration than the mono-interstitials, must be responsible.

Recent phase-field modelling by Gao et al. [45] suggested three mechanisms of cavity lattice formation under differing damage production and recombination rate regimes. Two involved spinodal decomposition; the first mechanism is accompanied by concomitant ordering during decomposition, with the lattice spacing being determined by the diffusivity of the SIA clusters; the second mechanism involves spinodal decomposition due to high mobility of vacancies (~ 10 times higher than the first mechanism) which gives rise to random void formation from the spinodal decomposition followed by ordering via recombination with anisotropically diffusing SIA clusters. These two mechanisms require defect production rates to be much larger than the recombination rate so that the vacancy concentration can enter the spinodal region leading to phase decomposition into voids. A recent work [46] has shown that d electron characteristics determine the defect properties of SP-CSAs composed of 3d transition metals and pointed out that defect energetics, including formation and migration energies, are critical to understanding and predicting irradiation-induced defect dynamics. The defect formation and migration energies in equiatomic NiCoCr and NiCrFeCo SP-CSAs have been calculated using density functional theory (DFT) [46]. Interestingly, both alloys are found to exhibit a large overlap region in distributions of migration energies for Cr/Fe interstitials and vacancies. These results indicate that interactions between interstitials and vacancies may be enhanced, leading to improved defect recombination in these equiatomic alloys. These higher recombination rates of defects predicted in these SP-CSAs as discussed,

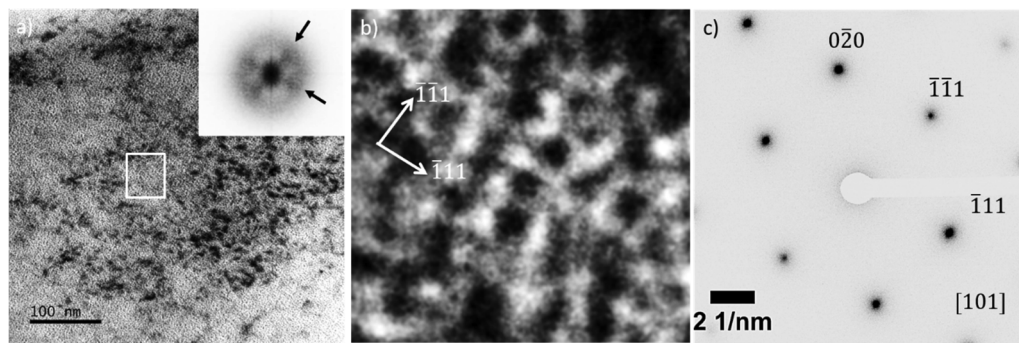


Fig. 5. FeNi sample irradiated with 3.2 keV He ions to a fluence of $3.2 \times 10^{17} \text{ ions/cm}^2$ at 298 K. (a) BF-TEM image of a helium bubble lattice taken with $1 \mu\text{m}$ of overfocus close to the [1 0 1] zone axis, FFT inset shows ‘lobes’ formed along $\langle 111 \rangle$ directions indicated by arrows, showing 2-D bubble alignment. (b) enlarged image of region inside white box in a. (c) SADP of region shown in a and b, in which shows the ‘lobes’ present in the FFT are associated with He bubble lattice ordering along $\langle 111 \rangle$ directions.

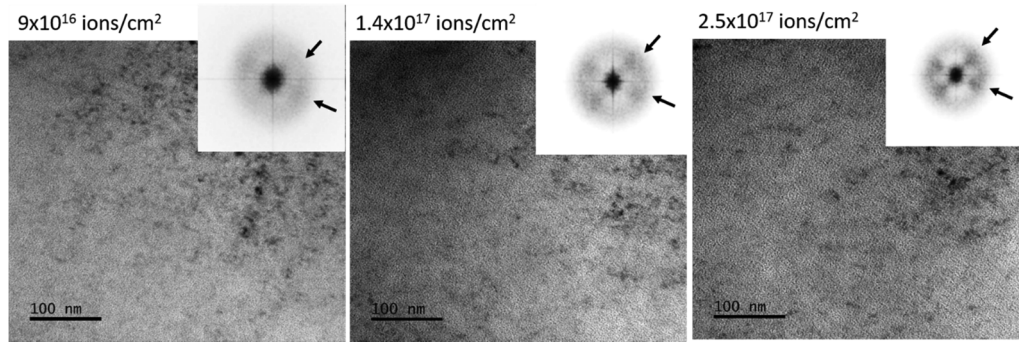


Fig. 6. Evolution of He bubble lattice ordering in a FeNi sample (imaged close to the [1 0 1] zone axis) as a function of increasing He ion fluence showing that lobes along $\langle 111 \rangle$ directions in the FFT (indicated by arrows) can be seen indicating an ordered bubble lattice that is observed at a fluence of 1.4×10^{17} ions/cm 2 and is clearly visible at a fluence of 2.5×10^{17} ions/cm 2 . Images record with 1 μm of overfocus.

along with the low temperature of irradiation, will be unlikely to lead to conditions that will permit entering the spinodal region. The observation in this work of bubble nucleation followed by bubble lattice formation and increased ordering with ion dose seemingly rules out the first mechanism suggested by Gao et al. [45] of phase decomposition with concurrent ordering. Equally, the low temperatures of the experiments implies low vacancy mobility, and this, coupled with the anticipated high recombination of defects in these alloys [10,47], means that it is not expected that the second mechanism reported by Gao et al. [45] will be active. The third mechanism discussed by Gao et al. [45] requires the nucleation of voids followed by ordering via 1-D SIA migration; and this mechanism can become active when the ratio of defect production rate to recombination rate is lower than for the other mechanisms. Therefore, the third mechanism is likely to be the one operating in this work. This work has shown that, as the number of alloying elements in these SP-CSAs increases, higher fluences (and thus time under equivalent irradiation conditions) are required to form bubble lattices. This clearly shows that ordering does not occur concomitantly with cavity nucleation but supports the mechanisms of random void nucleation with subsequent ordering via 1-D SIA diffusion. More importantly, it is clear that anisotropic diffusion of SIAs plays a critical role in the formation of cavity lattices and must, therefore, be active in these SP-CSAs.

4.2. Effect of chemical complexity on lattice formation

Fig. 9 shows a plot of the He bubble diameters for the Ni, FeNi and FeCrNiCo samples irradiated at 298 K as a function of fluence. It can be seen that for all samples, He bubble diameter increases with increasing fluence. However, it can also be seen that bubble diameters were much larger in the pure Ni samples than in the multi-component FeNi and FeCrNiCo alloys for the same fluence. Lu et al. [47] report a similar observation in void sizes in 1.5 MeV Ni-ion-irradiated Ni, FeNi and FeNiCo SP-CSAs which was attributed to the lower mobility of SIAs as alloy complexity is increased, leading to enhanced recombination with vacancies formed during the cascade and lower survival rates of Frenkel pairs (FPs). **Fig. 10** shows a plot of the He bubble lattice parameter as a function of fluence showing that the He bubble lattice parameter (a_{bubble}) in the pure Ni sample is around 9 nm, but is only 5–6 nm for the FeNi and FeCrNiCo samples. It is assumed that the majority of He atoms come to rest in irradiation induced vacancies as these are the dominant sinks for migrating He atoms. The number of vacancies formed per injected He ion is around 7 for each alloy composition from SRIM calculations [48] (based on E_d of all atoms being 40 eV). However, as alloy complexity is increased, FP survival rate decreases through increased interstitial-vacancy recombination [47], leading to a lower number of sinks for He. This may lead to the formation of He-vacancy clusters with a higher He/vacancy ratio for the same fluence of He ions as alloy complexity is increased, leading to decreased vacancy mobility

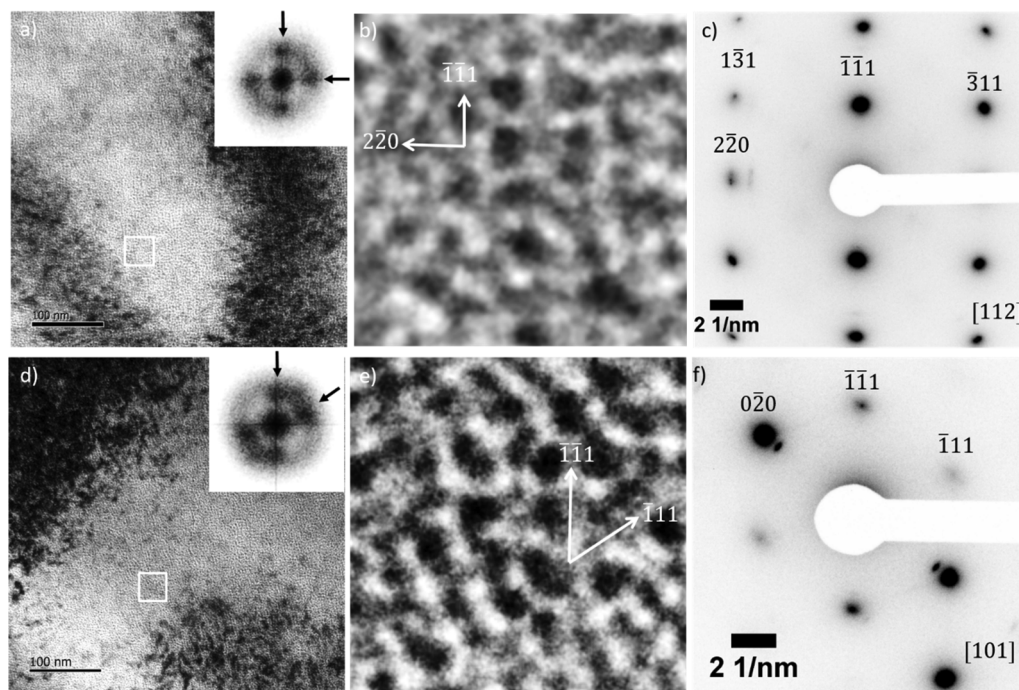


Fig. 7. FeCrNiCo sample irradiated with 30 keV He ions to a fluence of 4×10^{17} ions/cm 2 at 298 K. (a) BF-TEM image of He bubble lattice close to [1 1 2] zone axis taken with 1 μm of overfocus. Inset top right shows FFT. (b) enlarged image of region inside white box in a. (c) SADP of region shown in a and b, in which shows the “lobes” present in the FFT are associated with He bubble lattice ordering along $\langle 111 \rangle$ and $\langle 110 \rangle$ directions. (d) BF-TEM image of He bubble lattice close to [1 0 1] zone axis taken with 1 μm of overfocus. Inset top right shows FFT. (e) enlarged image of region inside white box in d. (f) SADP of region shown in d and e, in which shows the “lobes” present in the FFT are associated with He bubble lattice ordering along $\langle 111 \rangle$ directions.

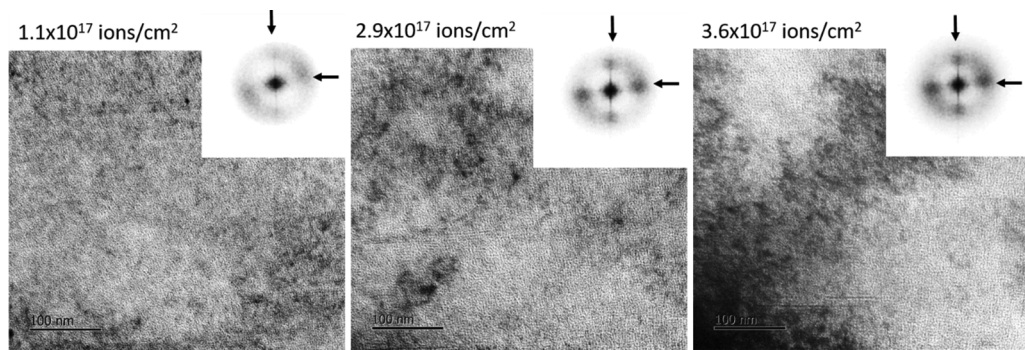


Fig. 8. Evolution of He bubble lattice ordering in a FeCrNiCo sample (imaged close to the [112] zone axis) as a function of increasing He ion fluence showing lobes in the FFT insets form along $\langle 111 \rangle$ directions an ordered lattice that can be seen at a fluence of $\sim 2.9 \times 10^{17}$ ions/cm 2 and which is more fully developed at a fluence of 3.6×10^{17} ions/cm 2 .

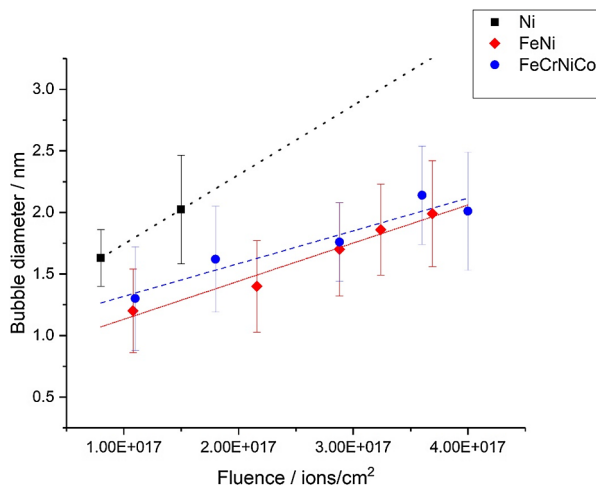


Fig. 9. He bubble diameter as a function of fluence for Ni, FeNi and FeCrNiCo samples irradiated with 30 keV He ions at RT at 298 K (lines to guide eyes only).

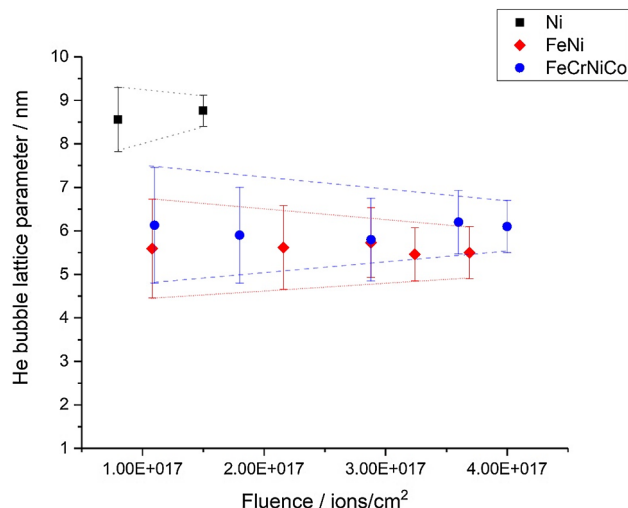


Fig. 10. He bubble lattice parameter as a function of fluence for Ni, FeNi and FeCrNiCo samples irradiated with 30 keV He ions at 298 K (lines to guide eyes only).

via a He pinning mechanism. This decrease in He-vacancy cluster mobility leads to smaller He bubble diameters when alloy chemical complexity is increased. Moreover, as vacancy pinning increases in the SP-CSAs (i.e. mobility decreases), a higher number density of smaller He bubbles nucleates resulting in a bubble lattice with a smaller lattice spacing when the SIA ordering mechanism occurs. Previous work [23] showed that He bubble lattice parameters in W decreased with higher He content due to increased vacancy pinning, agreeing well with the

current work. From Fig. 10 it can also be seen that, for low fluences ($< 2 \times 10^{17}$ ions/cm 2), the standard deviation of the measured He bubble lattice constant is lowest for the pure Ni samples, indicating a high degree of bubble ordering, whereas the variance is much higher for the FeNi and FeCrNiCo samples showing poor bubble ordering. This large variance of bubble lattice spacing in the FeNi and FeCrNiCo samples decreases with increasing fluence, showing that the bubble lattices become more ordered with increasing fluence, as seen in the FFTs shown in Section 3. A stark primary observation is that, for the bubble lattice ordering mechanism to occur, the fraction of surviving SIA atoms or clusters must undergo long range anisotropic SIA diffusion in the SP-CSAs; and secondly that bubble lattice ordering requires longer irradiation times and fluences to achieve a higher degree of bubble order in the SP-CSAs compared to pure Ni.

Lu et al. [47] used MD simulations to examine the diffusion migration pathways and mobility of interstitial defects in several multi-component equiatomic alloys (Ni, FeNi, FeNiCo, FeCrNiCo and FeCr-NiCoMn). The authors [47] reported the long range 1-D diffusion of interstitial clusters along $\langle 110 \rangle$ directions in Ni, which agrees well with the FCC cavity lattice formation as observed in this work. The migration energy of a di-interstitial (assumed to be the simplest active diffusing defect cluster in Ni in Ref. [32]) was reported to be 0.12 eV compared with 0.617 eV for the FeNi binary alloy; the difference being attributed to atomic size mismatch as well as the structural distortions from the random solid solution. In the case of FeNi, the interstitial clusters will migrate one-dimensionally along $\langle 110 \rangle$ directions; however, they were found to change orientation leading to 3-D migration along several $\langle 110 \rangle$ type directions. The authors [47] reported that in a 20 ns simulation the average distance travelled along a $\langle 110 \rangle$ direction was 1 nm before rotation onto another direction (giving 3-D migration) for the FeNi alloy at 1200 K. This distance is below that required for cavity lattice ordering reported in the work of Heinish and Singh [37] where the required 1-D SIA mean free path length for ordering is ~ 2.7 times the inter-cavity spacing which would equate to ~ 11 nm (~ 4 nm inter-bubble spacing) in this work. Although simple comparisons should not be made between 20 ns/ ~ 1 nm from the MD simulations and $\sim s/\sim 11$ nm experimental estimations, the influence of anisotropic chemical effects is clear. The increased change in migration direction giving 3-D diffusion in Ref. [47] was attributed to atomic level chemical heterogeneity, leading to lattice distortion and thus enhanced atomic scattering and decreased motion of interstitials along the close packed directions.

Zhao et al. [49] used DFT and MD simulations to study the defect formation and diffusion in FeNi CSAs. The authors [49] found that diffusion of SIA clusters in NiFe alloys is chemically biased with diffusion of Ni-Ni and Ni-Fe dumbbells being more likely than the Fe-Fe dumbbell due to their lower energy of formation. This diffusion, mainly via the Ni subsystem in the FeNi alloy may also enhance the change of direction of the dumbbell diffusion depending on the location of the nearest-neighbour Ni atoms. This agrees with the MD simulations performed by Osetsky et al. [50,52] to study the diffusion of defects in Ni,

Fe and NiFe CSA, again finding that diffusion was dominated by Ni-Ni dumbbells and that there was a preference for interstitials to maintain that composition. In pure Ni and Fe, the interstitial atom may jump to any of the 12 interstitial sites in the unit cell, however, in the FeNi alloy these directions are limited by the type of atom in the nearest site, where interstitial Ni atoms will preferentially jump to Ni sites, leading to the change in migration direction. Shi et al. [51] examined the 1-D motions of dislocation loops in pure Ni and Ni-containing CSAs (FeNi, NiCo, NiCoCr FeCrNiCo, FeCrNiCoMn and FeCrNiCoPd) using *in-situ* ion irradiation with 1 MeV Kr ions at 773 K. The authors [51] found that for loops < 10 nm in size (but still large enough to be easily resolved in the TEM), 1-D glide was observable in pure Ni and FeNi, NiCo and FeCrNiCo CSAs only. The directions of the loop glide were found to be along <1 1 0> directions and the average 1-D glide distance was 32, 8 and 3.5 nm for pure Ni, FeNi and FeCrNiCo, respectively. The jump frequency also decreased with alloy complexity from ~3/s for pure Ni to ~0.5/s for NiFe. These migration distances are much larger than those from the MD simulations in [47] and are also found for much larger diffusing defects (10 nm dislocation loops in [51] compared with SIA clusters [47]), but are on the same order of magnitude to produce a bubble lattice as described in [37]. Shi et al. [51] also reported that there were insufficient numbers of observations of loop glide direction changes to substantiate MD simulations in [47]. This may be due to a number of possible reasons: the lower temperature of the irradiations performed in [51] (773 K) compared to the MD simulations in [47] (1200 K); an effect of radiation enhanced mobility that gives rise to longer range in 1-D SIA migration paths; surface effects on the relatively thin TEM specimens; or uncertainty in the interatomic potential used in the MD simulations.

The increasing fluence and longer times needed to give rise to a comparable He bubble lattice in the FeNi and FeCrNiCo alloys, compared to that in the pure Ni may be due to the sluggish diffusion of SIA clusters, compared to the rapid 1-D diffusion of the SIAs in Ni. This is in good agreement with the MD simulations [47] showing that SIA migration distance decreased with alloy complexity and also agrees well with experimental observations of the 1-D dislocation loop glide distances and jump frequencies reported in [51]. Migration lengths of these defects in 1-D motion may also be increased by radiation enhanced diffusion, which is not taken into account in the thermally enhanced defect mobility simulations in Ref. [47]. However, it is also noted that higher fluences were required to achieve comparable He bubble diameters in the FeNi and FeCrNiCo alloys compared to the pure Ni. This may delay observable bubble ordering in the TEM as there may be an increasing number of small He-vacancy complexes which are beyond the resolution of the TEM at lower fluences.

5. Conclusions

Ni and equiatomic FeNi and FeCrNiCo alloys have been irradiated with 30 keV He⁺ ions at 298 K. Helium bubble superlattices are observed to form in all materials under these conditions. The sluggish chemically-biased defect diffusion in CSAs leads to smaller superlattice parameters with smaller bubble diameters. The details of the development of helium bubble superlattices in SP-CSAs and HEA systems highlight the unique chemical effects on anisotropic defect migration and microstructure evolution in these materials. The fluence required to produce He bubble ordering increased with increasing alloy complexity from ~8.0×10¹⁶ ions/cm² in pure Ni to ~1.1×10¹⁷ ions/cm² in FeCrNiCo. The predominant formation mechanism of helium bubble lattices requires the long range 1-D diffusion of SIAs. The SP-CSAs have been considered to have limited 1-D SIA diffusion lengths at high temperatures leading to slower defect accumulation and growth. However, the observation of He bubble lattices in these materials shows 1-D migration of SIA clusters is possible over increasingly longer irradiation time scales, even for complex alloys such as HEAs. This will have important consequences for defect kinetics in these complex

chemically inhomogeneous alloys.

Acknowledgements

RWH, HL, GG and SED are grateful to the EPSRC for financial support of this project (EP/M011135/1 and EP/M028283/1). YZ and HB were supported as part of the Energy Dissipation to Defect Evolution (EDDE), an Energy Frontier Research Center funded by the U.S. Department of Energy, Office of Science, Basic Energy Sciences under contract number DE-AC05-00OR22725.

References

- [1] B. Gludovatz, A. Hohenwarter, D. Catoor, E.H. Chang, E.P. George, R.O. Ritchie, A fracture-resistant high-entropy alloy for cryogenic applications, *Science* (80-) 345 (2014) 1153–1158, <https://doi.org/10.1126/science.1254581>.
- [2] D.B. Miracle, O.N. Senkov, A critical review of high entropy alloys and related concepts, *Acta Mater.* 122 (2017) 448–511, <https://doi.org/10.1016/j.actamat.2016.08.081>.
- [3] C. Xiang, J. Wang, H. Fu, E.-H. Han, H. Zhang, J. Wang, Z. Zhang, Corrosion behavior of several high-entropy alloys in high temperature high pressurewater, *J. Chinese Soc. Corros. Prot.* 36 (2016) 107–112, <https://doi.org/10.11902/1005.4537.2016.024>.
- [4] Y. Shi, B. Yang, P. Liaw, Corrosion-resistant high-entropy alloys: a review, *Metals (Basel)*. 7 (2017) 43, <https://doi.org/10.3390/met7020043>.
- [5] Y. Qiu, S. Thomas, M.A. Gibson, H.L. Fraser, N. Birbilis, Corrosion of high entropy alloys, *Npj Mater. Degrad.* 1 (2017) 15, <https://doi.org/10.1038/s41529-017-0009-y>.
- [6] Y. Qiu, M.A. Gibson, H.L. Fraser, N. Birbilis, Corrosion characteristics of high entropy alloys, *Mater. Sci. Technol.* 31 (2015) 1235–1243, <https://doi.org/10.1179/1743284715Y.0000000026>.
- [7] C.P. Lee, C.C. Chang, Y.Y. Chen, J.W. Yeh, H.C. Shih, Effect of the aluminium content of AlxCrFe1.5MnNi0.5 high-entropy alloys on the corrosion behaviour in aqueous environments, *Corros. Sci.* 50 (2008) 2053–2060, <https://doi.org/10.1016/j.corsci.2008.04.011>.
- [8] Y.Y. Chen, T. Duval, U.D. Hung, J.W. Yeh, H.C. Shih, Microstructure and electrochemical properties of high entropy alloys—a comparison with type-304 stainless steel, *Corros. Sci.* 47 (2005) 2257–2279, <https://doi.org/10.1016/j.corsci.2004.11.008>.
- [9] Y.Y. Chen, U.T. Hong, H.C. Shih, J.W. Yeh, T. Duval, Electrochemical kinetics of the high entropy alloys in aqueous environments—a comparison with type 304 stainless steel, *Corros. Sci.* 47 (2005) 2679–2699, <https://doi.org/10.1016/j.corsci.2004.09.026>.
- [10] C. Lu, T. Yang, K. Jin, N. Gao, P. Xiu, Y. Zhang, F. Gao, H. Bei, W.J. Weber, K. Sun, Y. Dong, L. Wang, Radiation-induced segregation on defect clusters in single-phase concentrated solid-solution alloys, *Acta Mater.* 127 (2017) 98–107, <https://doi.org/10.1016/j.actamat.2017.01.019>.
- [11] M.R. He, S. Wang, S. Shi, K. Jin, H. Bei, K. Yasuda, S. Matsumura, K. Higashida, I.M. Robertson, Mechanisms of radiation-induced segregation in CrFeCoNi-based single-phase concentrated solid solution alloys, *Acta Mater.* 126 (2017) 182–193, <https://doi.org/10.1016/j.actamat.2016.12.046>.
- [12] Y. Zhang, G.M. Stocks, K. Jin, C. Lu, H. Bei, B.C. Sales, L. Wang, L.K. Béland, R.E. Stoller, G.D. Samolyuk, M. Caro, A. Caro, W.J. Weber, Influence of chemical disorder on energy dissipation and defect evolution in concentrated solid solution alloys, *Nat. Commun.* 6 (2015) 8736, <https://doi.org/10.1038/ncomms9736>.
- [13] P.B. Johnson, D.J. Mazey, Gas-bubble superlattice formation in bcc metals, *J. Nucl. Mater.* 218 (1995) 273–288, [https://doi.org/10.1016/0022-3115\(94\)00674-1](https://doi.org/10.1016/0022-3115(94)00674-1).
- [14] P. Johnson, D. Mazey, Helium gas-bubble superlattice in copper and nickel, *Nature*. 281 (1979) 359–360, <https://doi.org/10.1038/281359a0>.
- [15] K. Krishan, Invited review article ordering of voids and gas bubbles in radiation environments, *Radiat. Eff.* 66 (1982) 121–155, <https://doi.org/10.1080/00337578208222474>.
- [16] J.H. Evans, Observations of a regular void array in high purity molybdenum irradiated with 2 MeV nitrogen ions, *Nature*. 229 (1971) 403–404.
- [17] P.B. Johnson, D.J. Mazey, Helium gas bubble lattices in face-centred-cubic metals, *Nature*. 276 (1978) 595–596.
- [18] T. Tanno, A. Hasegawa, J.C. He, M. Fujiwara, M. Satou, S. Nogami, K. Abe, T. Shishido, Effects of transmutation elements on the microstructural evolution and electrical resistivity of neutron-irradiated tungsten, *J. Nucl. Mater.* 386–388 (2009) 218–221, <https://doi.org/10.1016/j.jnucmat.2008.12.091>.
- [19] T. Tanno, A. Hasegawa, J.-C. He, M. Fujiwara, S. Nogami, M. Satou, T. Shishido, K. Abe, Effects of transmutation elements on neutron irradiation hardening of tungsten, *Mater. Trans.* 48 (2007) 2399–2402, <https://doi.org/10.2320/matertrans.MAW200722>.
- [20] G.S. Was, Fundamentals of Radiation Materials Science, first ed., Springer-Verlag, Berlin Heidelberg, New York, 2007, , <https://doi.org/10.1017/CBO9781107415324.004>.
- [21] V.K. Sikka, J. Mottef, Superlattice of voids in neutron-irradiated tungsten, *J. Appl. Phys.* 43 (1972) 4942–4944, <https://doi.org/10.1063/1.1661050>.
- [22] A.M. Robinson, P.D. Edmondson, C. English, S. Lazano-Perez, G. Greaves, J.A. Hinks, S.E. Donnelly, C.R.M. Grovenor, The effect of temperature on bubble lattice formation in copper under *in situ* He ion irradiation, *Scr. Mater.* 131 (2017)

- 108–111.
- [23] R.W. Harrison, G. Greaves, J.A. Hinks, S.E. Donnelly, Engineering self-organising helium bubble lattices in tungsten, *Sci. Rep.* 7 (2017) 7724.
- [24] R.W. Harrison, G. Greaves, J.A. Hinks, S.E. Donnelly, A study of the effect of helium concentration and displacement damage on the microstructure of tungsten irradiation with helium ions, *J. Nucl. Mater.* 495 (2017) 492–503.
- [25] R.W. Harrison, H. Amari, G. Greaves, J.A. Hinks, S.E. Donnelly, Effect of He-appm/DPA ratio on the damage microstructure of tungsten, *MRS Adv.* 1 (2016) 2893–2899, <https://doi.org/10.1557/adv.2016.385>.
- [26] V.I. Dubinko, A.V. Tur, A.A. Turkin, V.V. Yanovskij, A mechanism of formation and properties of the void lattice in metals under irradiation, *J. Nucl. Mater.* 161 (1989) 57–71, [https://doi.org/10.1016/0022-3115\(89\)90462-5](https://doi.org/10.1016/0022-3115(89)90462-5).
- [27] C.H. Woo, W. Frank, A Theory of Void Lattice Formation, *J. Nucl. Mater.* 137 (1985) 7–21.
- [28] J.H. Evans, Void and bubble lattice formation in molybdenum: A mechanism based on two-dimensional self-interstitial diffusion, *J. Nucl. Mater.* 119 (1983) 180–188, [https://doi.org/10.1016/0022-3115\(83\)90195-2](https://doi.org/10.1016/0022-3115(83)90195-2).
- [29] D.J. Mazey, B.L. Eyre, J.H. Evans, S.K. Erents, G.M. McCracken, A transmission electron microscopy study of molybdenum irradiated with helium ions, *J. Nucl. Mater.* 64 (1977) 145–156, [https://doi.org/10.1016/0022-3115\(77\)90018-6](https://doi.org/10.1016/0022-3115(77)90018-6).
- [30] J.H.J. Evans, A computer simulation of the two-dimensional SIA diffusion model for void lattice formation, *J. Nucl. Mater.* 132 (1985) 147–155, [https://doi.org/10.1016/0022-3115\(85\)90408-8](https://doi.org/10.1016/0022-3115(85)90408-8).
- [31] P.B. Johnson, D.J. Mazey, J.H. Evans, Bubble structures in He + irradiated metals, *Radiat. Eff.* 78 (1983) 147–156, <https://doi.org/10.1080/00337578308207367>.
- [32] J.H.J. Evans, Simulations of the effects of 2-D interstitial diffusion on void lattice formation during irradiation, *Philos. Mag.* 86 (2006) 173–188, <https://doi.org/10.1080/14786430500380134>.
- [33] P.B. Johnson, Gas Bubble Lattices in Metals - Fundamental Aspects of Inert Gases in Solids, Springer, US, Boston, MA, 1991, pp. 167–184, , https://doi.org/10.1007/978-1-4899-3680-6_14.
- [34] V. Tewary, R. Bulloough, Theory of the void lattice in molybdenum, *J. Phys. F Met. Phys.* 69 (1972) L68–L72, <https://doi.org/10.1088/0305-4608/2/4/001>.
- [35] A.G. Khachaturyan, V.M. Airapetyan, Spatially periodic distributions of new phase inclusions caused by elastic distortions, *Phys. Status Solidi.* 26 (1974) 61–70, <https://doi.org/10.1002/pssa.2210260104>.
- [36] V.I. Dubinko, V.V. Slezov, A.V. Tur, V.V. Yanovsky, The theory of gas bubble lattice, *Radiat. Eff.* 100 (1986) 85–104, <https://doi.org/10.1080/00337578608208738>.
- [37] H.L. Heinisch, B.N. Singh, The effects of one-dimensional migration of self-interstitial clusters on the formation of void lattices, *J. Nucl. Mater.* 307–311 (2002) 876–880, [https://doi.org/10.1016/S0022-3115\(02\)01005-X](https://doi.org/10.1016/S0022-3115(02)01005-X).
- [38] G. Greaves, A.H. Mir, R.W. Harrison, M.A. Tunstall, S.E. Donnelly, J.A. Hinks, New Microscope And Ion Accelerators For Materials Investigations (MIAMI-2) system at the University of Huddersfield, *Nucl. Instruments Methods Phys. Res. Sect. A Accel. Spectrometers Detect. Assoc. Equip.* 931 (2019) 37–43, <https://doi.org/10.1016/j.nima.2019.03.074>.
- [39] M. Heideman, D. Johnson, C. Burrus, Gauss and the history of the fast Fourier transform, *IEEE ASSP Mag.* 1 (1984) 14–21, <https://doi.org/10.1109/MASSP.1984.1162257>.
- [40] P.M. Derlet, D. Nguyen-Manh, S.L. Dudarev, Multiscale modeling of crowdion and vacancy defects in body-centered-cubic transition metals, *Phys. Rev. B.* 76 (2007) 54107, <https://doi.org/10.1103/PhysRevB.76.054107>.
- [41] D. Nguyen-Manh, A.P. Horsfield, S.L. Dudarev, Self-interstitial atom defects in bcc transition metals: group-specific trends, *Phys. Rev. B.* 73 (2006) 20101.
- [42] D. Nguyen-Manh, S.L. Dudarev, A.P. Horsfield, Systematic group-specific trends for point defects in bcc transition metals: an ab initio study, *J. Nucl. Mater.* 367–370 A (2007) 257–262, <https://doi.org/10.1016/j.jnucmat.2007.03.006>.
- [43] P.B. Johnson, A.L. Malcolm, D.J. Mazey, Importance of stress in bubble ordering in the helium gas-bubble superlattice in copper, *Nature* 329 (1987) 316–318.
- [44] J.R. Beeler JR., 5 - Self interstitials - Radiation Effects Computer Experiments, Defects in Solids, Elsevier, Oxford, 1983, pp. 207–315, , <https://doi.org/10.1016/B978-0-444-86315-7.50009-0>.
- [45] Y. Gao, Y. Zhang, D. Schwen, C. Jiang, C. Sun, J. Gan, Formation and self-organization of void superlattices under irradiation: a phase field study, *Materialia* 1 (2018) 78–88, <https://doi.org/10.1016/j.mtla.2018.04.003>.
- [46] S. Zhao, T. Egami, G.M. Stocks, Y. Zhang, Effect of d electrons on defect properties in equiatomic NiCoCr and NiCoFeCr concentrated solid solution alloys, *Phys. Rev. Mater.* 2 (2018) 013602, , <https://doi.org/10.1103/PhysRevMaterials.2.013602>.
- [47] C. Lu, L. Niu, N. Chen, K. Jin, T. Yang, P. Xiu, Y. Zhang, F. Gao, H. Bei, S. Shi, M.R. He, I.M. Robertson, W.J. Weber, L. Wang, Enhancing radiation tolerance by controlling defect mobility and migration pathways in multicomponent single-phase alloys, *Nat. Commun.* 7 (2016) 1–8, <https://doi.org/10.1038/ncomms13564>.
- [48] J.F. Ziegler, SRIM-2003, Nucl. Instruments Methods Phys. Res. Sect. B Beam Interact. Mater. Atoms. 219–220 (2004) 1027–1036, <https://doi.org/10.1016/j.nimb.2004.01.208>.
- [49] S. Zhao, Y. Ossetsky, Y. Zhang, Preferential diffusion in concentrated solid solution alloys: NiFe, NiCo and NiCoCr, *Acta Mater.* 128 (2017) 391–399, <https://doi.org/10.1016/j.actamat.2017.01.056>.
- [50] Y.N. Ossetsky, L.K. Béland, R.E. Stoller, Specific features of defect and mass transport in concentrated fcc alloys, *Acta Mater.* 115 (2016) 364–371, <https://doi.org/10.1016/j.actamat.2016.06.018>.
- [51] S. Shi, H. Bei, I.M. Robertson, Impact of alloy composition on one-dimensional glide of small dislocation loops in concentrated solid solution alloys, *Mater. Sci. Eng. A.* 700 (2017) 617–621, <https://doi.org/10.1016/j.msea.2017.05.049>.
- [52] Y.N. Ossetsky, L. Béland, A. Barashev, Y. Zhang, On the existence and origin of sluggish diffusion in chemically disordered concentrated alloys, *Curr. Opin. Solid State Mater. Sci.* 22 (2018) 65–74.